

## Research Paper

# Non-invasive monitoring of *in vivo* hydrogel degradation and cartilage regeneration by multiparametric MR imaging

Zelong Chen<sup>1\*</sup>, Chenggong Yan<sup>1\*</sup>, Shina Yan<sup>2</sup>, Qin Liu<sup>1</sup>, Meirong Hou<sup>1</sup>, Yikai Xu<sup>1✉</sup>, Rui Guo<sup>2✉</sup>

1. Department of Medical Imaging Center, Nanfang Hospital, Southern Medical University, Guangzhou 510515, China;
2. Key Laboratory of Biomaterials of Guangdong Higher Education Institutes, Department of Biomedical Engineering, Jinan University, Guangzhou 510632, China.

\* These two authors contributed equally to this work.

✉ Corresponding author: guorui@jnu.edu.cn, yikaixu917@gmail.com

© Ivyspring International Publisher. This is an open access article distributed under the terms of the Creative Commons Attribution (CC BY-NC) license (<https://creativecommons.org/licenses/by-nc/4.0/>). See <http://ivyspring.com/terms> for full terms and conditions.

Received: 2017.08.24; Accepted: 2017.11.25; Published: 2018.01.13

## Abstract

Numerous biodegradable hydrogels for cartilage regeneration have been widely used in the field of tissue engineering. However, to non-invasively monitor hydrogel degradation and efficiently evaluate cartilage restoration *in situ* is still challenging.

**Methods:** A ultrasmall superparamagnetic iron oxide (USPIO)-labeled cellulose nanocrystal (CNC)/silk fibroin (SF)-blended hydrogel system was developed to monitor hydrogel degradation during cartilage regeneration. The physicochemical characterization and biocompatibility of the hydrogel were evaluated *in vitro*. The *in vivo* hydrogel degradation and cartilage regeneration of different implants were assessed using multiparametric magnetic resonance imaging (MRI) and further confirmed by histological analysis in a rabbit cartilage defect model for 3 months.

**Results:** USPIO-labeled hydrogels showed sufficient MR contrast enhancement and retained stability without loss of the relaxation rate. Neither the mechanical properties of the hydrogels nor the proliferation of bone-marrow mesenchymal stem cells (BMSCs) were affected by USPIO labeling *in vitro*. CNC/SF hydrogels with BMSCs degraded more quickly than the acellular hydrogels as reflected by the MR relaxation rate trends *in vivo*. The morphology of neocartilage was noninvasively visualized by the three-dimensional water-selective cartilage MRI scan sequence, and the cartilage repair was further demonstrated by macroscopic and histological observations.

**Conclusion:** This USPIO-labeled CNC/SF hydrogel system provides a new perspective on image-guided tissue engineering for cartilage regeneration.

Key words: non-invasive monitoring, ultrasmall superparamagnetic iron oxide (USPIO), magnetic resonance imaging, hydrogel degradation, cartilage regeneration

## Introduction

Damaged articular cartilage caused by osteoarthritis or trauma rarely achieves complete self-repair because the tissue is avascular with simple cellularity. Despite surgical intervention, regenerated hyaline cartilage does not allow the recovery of joint function.<sup>[1-3]</sup> Consequently, construction strategies for cartilage regeneration are always a high-priority issue

in tissue engineering.<sup>[4-6]</sup> Ideal biomaterials for cartilage tissue engineering (CTE) should degrade at a moderate rate to coincide with cartilage regeneration, which is critical to maintain the mechanical properties and structural integrity of the joint.<sup>[7-12]</sup> In recent decades, numerous natural or synthetic biodegradable hydrogels composed of cells and

bioactive factors have been successfully designed for cartilage restoration.<sup>[13-15]</sup> However, researches on longitudinally and nondestructively tracking the processes of biomaterial degradation *in vivo* are limited. Zhang et al. demonstrated that fluorescently-labeled hyaluronan hydrogels, which were implanted into the spinal cord of mice, were feasible to reflect the *in vivo* degradation process.<sup>[16]</sup> Noninvasive monitoring of hydrogel degradation and cartilage regeneration in CTE remains to be explored.

Noninvasive imaging modalities could be powerful tools, providing efficient feedback on the real-time degradation of tissue engineering constructs *in situ*.<sup>[17-19]</sup> Because magnetic resonance imaging (MRI) is characterized by its safety, diverse functional sequences, excellent soft-tissue contrast, and penetration depth, it is widely used to monitor the molecular and functional changes that occur during biomaterial resorption and neo-tissue remodeling. The former has been monitored previously by diamagnetic chemical exchange saturation transfer (CEST) to demonstrate the distribution of the hydrogel filling in stroke cavities, and by cardiac MRI to determine the regional myocardial properties of injectable hydrogels.<sup>[20, 21]</sup> The latter has been evaluated by magnetic resonance elastography to evaluate the tissue mechanical properties, by sodium MRI to detect the proteoglycan concentration in tissue-engineered cartilage, as well as by relaxation times and diffusion coefficients to assess the composition of bladder acellular matrix-based scaffolds.<sup>[22-24]</sup> Furthermore, ultrasmall superparamagnetic iron oxide (USPIO) has rapidly emerged as a promising contrast agent in molecular MR imaging for tissue engineering. Due to its biocompatibility and superparamagnetic properties, USPIO has been intensively investigated as a functional tool for cancer detection, drug delivery monitoring, stem cells tracking and implanted scaffolds labeling.<sup>[25-34]</sup> Non-invasive monitoring approaches can help reduce the number of animals used: the experimental data can be achieved repeatedly to prevent unnecessary sacrifice for histological analysis at different time points. Additionally, the non-invasive and successive observations can provide efficient information and minimize individual differences between animals, which might facilitate the clinical translation of tissue engineering.

However, to the best of our knowledge, few investigations of efficient, truly real-time evaluation of hydrogel absorption and cartilage regeneration *in situ* have been reported. Here, we have developed for the first time a visualizable, functional USPIO-labeled cellulose nanocrystal (CNC)/silk fibroin (SF)

composite hydrogel system with which to semiquantitatively monitor the cartilage degradation process and clarify the hyaline cartilage regeneration using multiparametric MRI *in situ*. This system might provide meaningful insight into the noninvasive monitoring and longitudinal therapeutic efficacy of implanted hydrogels in CTE (Figure 1).

## Results and Discussion

### Synthesis of USPIO-labeled CNC/SF hydrogel

CTE strategies provide suitable environments to stimulate *in vivo* cartilage development, namely chondrogenesis, mainly including mesenchymal/precartilaginous condensation, interzone formation, cavitation and stabilization of articular cartilage.<sup>[4]</sup> SF is a natural protein widely used in cartilage repair because it not only acts as a three-dimensional (3D) architectural template for cell adhesion and proliferation, based on its excellent biocompatibility, but also provides good mechanical protection before neocartilage formation.<sup>[35]</sup> The unique secondary structures within SF (hydrophobic anti-parallel  $\beta$ -sheet and hydrophilic random coil) contribute to the mechanical property and elasticity enhancement.<sup>[36]</sup> Incorporated rod-shaped CNCs also reinforce the mechanical strength of CTE constructs.<sup>[37-39]</sup> The average length and diameter of the rod-like CNCs produced by the sulfuric acid hydrolysis of microcrystalline cellulose (MCC) were  $62.8 \pm 7.3$  nm and  $8.1 \pm 1.7$  nm, respectively (Figure S1A). Moreover, deleterious dose-dependent and target-cell-dependent effects of SPIO on the chondrogenic capacity have been detected *in vitro*. Previous studies demonstrated that SPIO labeling concentrations higher than  $25 \mu\text{g Fe/mL}$  showed inhibiting effect on chondrogenesis of hBMSCs and cell proliferation was affected in SPIO-labeled neonatal chondrocytes but not in hBMSCs or mature chondrocytes.<sup>[40, 41]</sup> Therefore, in this study, we explored the effects of USPIO-labeled CNC/SF hydrogel on the chondrogenesis of bone marrow mesenchymal stem cells (BMSCs) *in vitro* and on cartilage regeneration *in vivo*. The morphology of USPIO was observed with transmission electron microscopy (TEM) (Figure S1B). The diameter of the USPIO particles was  $\sim 15.7 \pm 2.0$  nm. The sol-gel transition of the hydrogels with incorporated USPIO occurred at room temperature (Figure S1C1-C3). Lyophilized hydrogel composites blended with USPIO, at concentrations ranging from 0% to 0.6% (w/w), were successfully fabricated for the *in vitro* assays. The non-labeled hydrogel was white, whereas the USPIO-labeled hydrogels were darker (Figure 2A).

## USPIO optimization of the labeled CNC/SF hydrogels

The optimal USPIO concentration was determined by structural analysis, MR visualization and cytotoxicity assay of the composite hydrogels. In this study, scanning electron microscopy (SEM) demonstrated mesh pore interconnectivity and uneven oval pores, ranging from  $78.3 \pm 21.7 \mu\text{m}$  to  $85.1 \pm 22.4 \mu\text{m}$ , in cross-sections of non-labeled and USPIO-labeled CNC/SF hydrogels (Figure 2A). As reported previously, hydrogels with pore sizes in the range of 70–250  $\mu\text{m}$  effectively promoted chondrogenesis.<sup>[42–44]</sup> No significant differences were found in the average pore sizes of the prepared hydrogels (Table S1). The USPIO concentration had no effect on the porosity and interconnectivity of the hydrogels, which was consistent with the previous report.<sup>[32]</sup>

Hydrogels were then scanned with T2-weighted imaging (T2WI), T2 mapping and T2\* mapping sequences to determine the image features and relaxation rates, respectively. No obvious magnetic susceptibility artifacts or deformations were observed below a USPIO concentration of 0.6% (w/w). The non-labeled hydrogels were hyperintense on T2WI, whereas the USPIO-labeled hydrogels were hypointense with a clear border (Figure 2A). The signal contrast in the prepared hydrogels gradually increased as the amount of USPIO increased. The corresponding relaxation rates of the USPIO-labeled hydrogels were then calculated. The R2 values

increased significantly, ranging from  $8.412 \pm 0.7031 \text{ s}^{-1}$  to  $25.67 \pm 2.455 \text{ s}^{-1}$  as the USPIO concentration increased, and R2\* showed a similar trend, ranging from  $52.19 \pm 1.215 \text{ s}^{-1}$  to  $133.33 \pm 4.406 \text{ s}^{-1}$  (Figure 2B). It is noteworthy that a linear relationship and high correlation were demonstrated between the USPIO content and the relaxation rate ( $r^2$  correlation coefficients and p values: 0.983 and  $< 0.001$ , respectively for R2; and 0.978 and  $< 0.001$ , respectively, for R2\*). Hydrogels with USPIO amounts lower than 0.6% (w/w) demonstrated no magnetic susceptibility artifacts caused by excessive USPIO incorporation<sup>[32]</sup> and were feasible for semiquantitative relaxation rate measurement. The iron content within the different hydrogels was confirmed with an inductively coupled plasma mass spectrometry (ICP-MS) analysis (Table S1), and the iron distribution within the different hydrogels was detected with Prussian blue staining (Figure 2A).

Then the cytotoxicity of all the prepared hydrogels was determined with Cell Counting Kit-8 assay (Figure 2C). No significant differences in cell viability were observed among the prepared hydrogels at different time points. The hydrogel with the least USPIO showed the closest optical density values to those of the non-labeled hydrogel over time. Therefore, 0.1% (w/w) USPIO-labeled CNC/SF hydrogel was used for the subsequent *in vitro* and *in vivo* assays because it displayed sufficient MR contrast and the best biocompatibility.

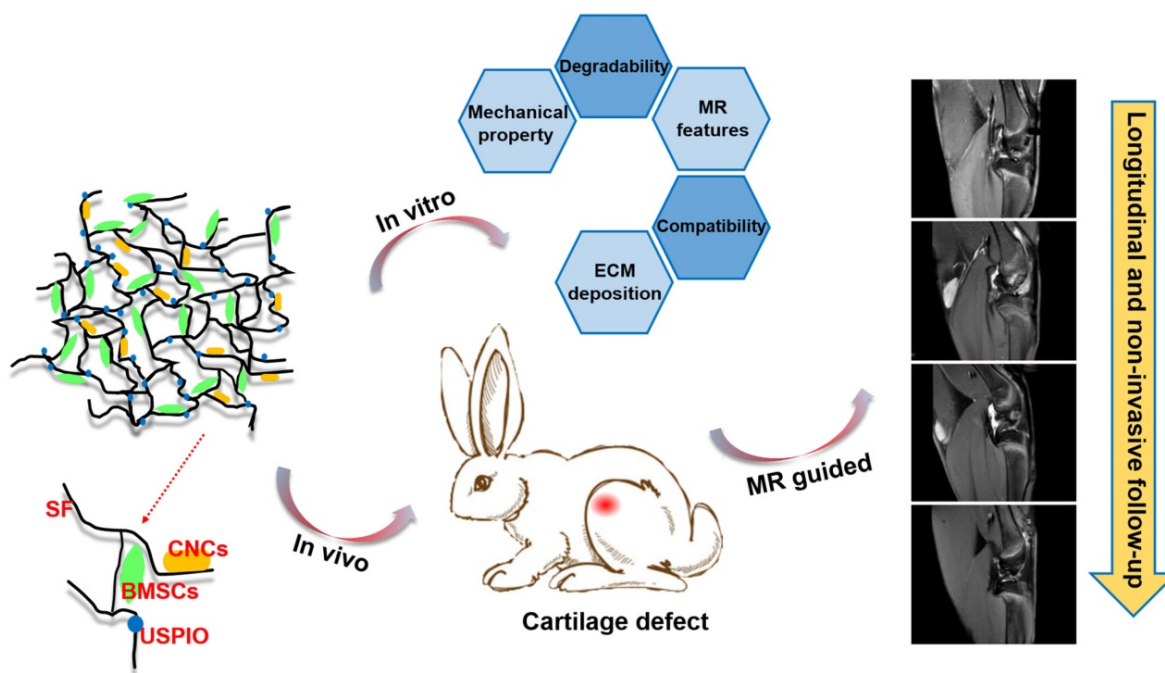


**Figure 1.** Schematic illustration of the experimental protocol. USPIO-labeled CNC/SF hydrogel system for cartilage tissue engineering was analyzed with *in vitro* assays and in an *in vivo* cartilage defect model.

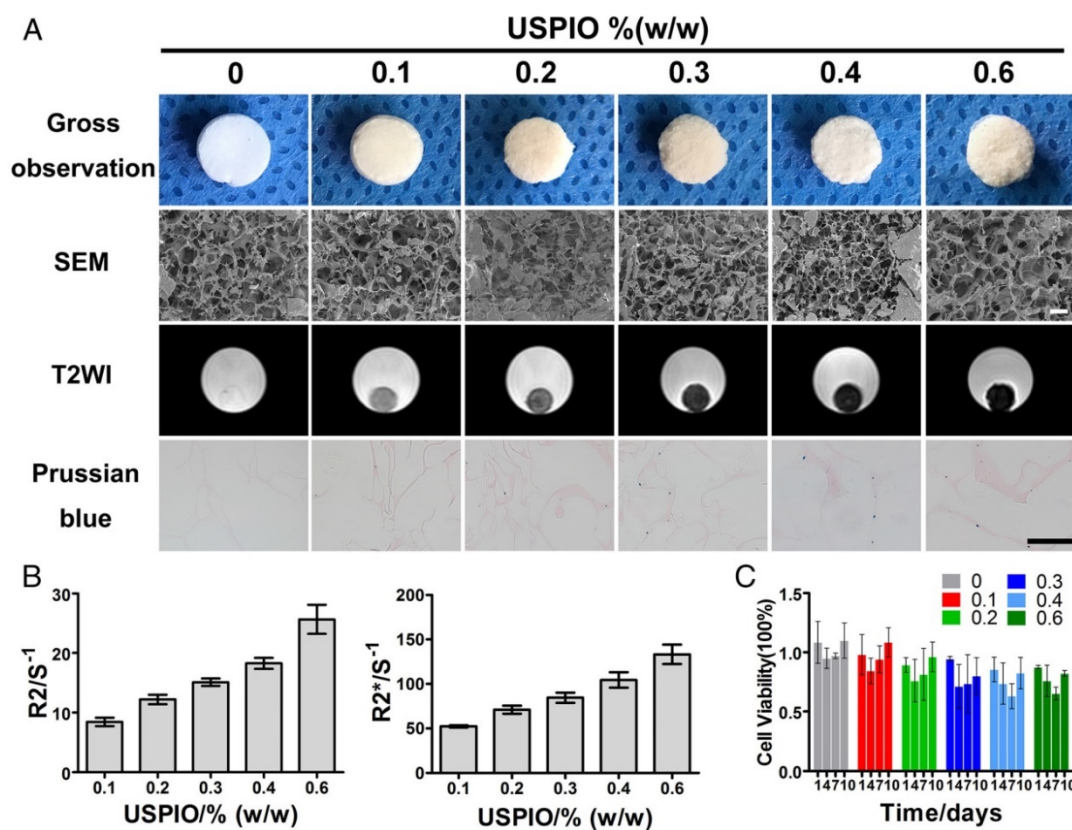


**Figure 2.** MRI characterization and structural observation of CNC/SF hydrogels with incorporated USPIO concentrations ranging from 0% to 0.6% (w/w). (A) SEM showed the uniform porosity and interconnected architecture of the USPIO-labeled SF/CNC hydrogels. T2-weighted imaging demonstrated that the signal contrast in the prepared hydrogels gradually improved with increasing amounts of USPIO. Prussian blue staining confirmed the incorporation of USPIO. Scale bar indicates 100  $\mu\text{m}$  for SEM and 50  $\mu\text{m}$  for Prussian blue staining. (B) R2 and R2\* relaxometry rates indicated that the USPIO content increased linearly. (C) Cytotoxicity results showed no negative effect resulting from the increasing USPIO concentration.

## Characterizations of the prepared SF/CNC hydrogels

Several physicochemical parameters of the composite hydrogels were also evaluated. The Fourier transform infrared spectroscopy (FT-IR) spectra of SF, CNC, CNC/SF, USPIO, and the USPIO/CNC/SF composites were determined (Figure 3A). The presence of crystal conformations within SF was demonstrated by absorption bands at 1661  $\text{cm}^{-1}$ , 1532  $\text{cm}^{-1}$ , and 1243  $\text{cm}^{-1}$ , which were attributed to amide I, amide II, and amide III groups, respectively. Compared with SF, CNC/SF had other characteristic absorbance peaks at 3345  $\text{cm}^{-1}$  due to O-H stretching, 2903  $\text{cm}^{-1}$ , 1433  $\text{cm}^{-1}$ , and 1323  $\text{cm}^{-1}$  due to  $-\text{CH}_2$ -stretching, and 1058  $\text{cm}^{-1}$  due to C-O stretching vibrations. Another characteristic band at 565  $\text{cm}^{-1}$  confirmed the corresponding stretching vibrations of Fe-O species within USPIO/CNC/SF. The mechanical properties of the SF, CNC/SF, and USPIO/CNC/SF hydrogels were examined and representative stress-strain curves were plotted (Figure 3B). At the same strain level, CNC/SF and USPIO/CNC/SF sustained much higher stress than the pure SF hydrogel. For example, the stress at

maximal strain was 194.09 $\pm$ 0.79 kPa for the SF hydrogel, 263.04 $\pm$ 0.95 kPa for the CNC/SF hydrogel, and 249.15 $\pm$ 1.32 kPa for the USPIO/CNC/SF hydrogels. These results indicate that CNCs improved the mechanical performance of tissue-engineered constructs, which is consistent with earlier studies.<sup>[37-39]</sup> However, the stress curve for the USPIO/CNC/SF hydrogel showed no mechanical enhancement vs. the CNC/SF hydrogel, which might be due to the low concentration of USPIO. The *in vitro* degradation behaviors of the hydrogels were also examined (Figure 3C). The percentage of the mass remaining on day 7 in the SF, CNC/SF, and USPIO/CNC/SF groups was 6.89 $\pm$ 1.08%, 10.6 $\pm$ 0.82%, and 11.54 $\pm$ 1.18%, respectively. No significant difference in the residual mass was observed between the CNC/SF and USPIO/CNC/SF hydrogels because the USPIO content was low. The thermal stability of the hydrogels was evaluated with a thermogravimetric analysis (Figure 3D). The results showed that similar masses of the CNC/SF and USPIO/CNC/SF hydrogels remained after treatment at 800  $^{\circ}\text{C}$ , which were greater than the remaining mass of SF. USPIO incorporation had no negative effect on the thermal stability of the hydrogel.

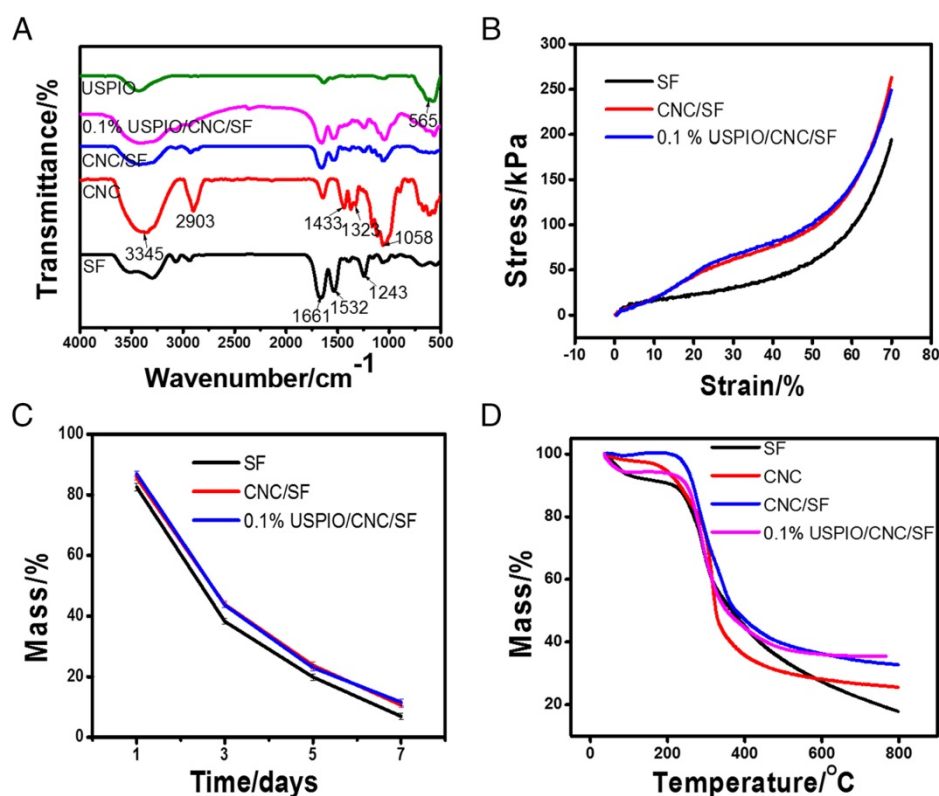


**Figure 3.** Physicochemical characterizations of CNC/SF hydrogels incorporating USPIO nanoparticles. (A) Fourier transform infrared spectroscopy. (B) Mechanical properties. (C) Degradation assay. (D) Thermogravimetric analysis.

### BMSCs viability, morphology and chondrogenesis evaluation *in vitro*

The viability and morphology of the BMSCs was evaluated with live/dead staining (Figure 4A1–A4). Most BMSCs attaching to the non-labeled or USPIO-labeled hydrogels remained viable (green), although a few overtly dead cells (red) were observed on day 14. On day 4, the BMSCs were spindle-shaped and flat, and aggregated into condensed clusters, which was essential for their chondrogenic differentiation.<sup>[45]</sup> Interestingly, the BMSCs gradually adopted a spheroid shape, which indicated their differentiation into chondrocytes. Additionally, the extracellular matrix (ECM) deposition in non-labeled and USPIO-labeled CNC/SF hydrogels was observed with SEM after BMSCs seeding for 4 and 14 days (Figure 4B1–B4). On day 4, only the BMSCs were found adhering to hydrogels, while abundant ECM deposited in the porous interstices of the hydrogels in both groups on day 14.

The total glycosaminoglycan (GAG) contents of non-labeled or USPIO-labeled CNC/SF hydrogels, normalized to the DNA content, showed a robust and sustained increase, reaching a peak of approximately three-fold the initial concentration on day 28. The DNA content, consistent with cell proliferation, remained at a high level over time (Figure S2A).

Hematoxylin–eosin (H&E) and toluidine blue staining were used to investigate the cell attachment and ECM secretion during *in vitro* chondrogenesis on days 14 and 28, respectively. H&E staining showed that the BMSCs seeded in both groups were distributed either in a dispersed pattern or in clusters within the mesh interstices (Figure 4C1–C4). Toluidine-blue-positive areas clearly indicated that ECM accumulation increased gradually over time, in parallel with the GAG content (Figure 4D1–D4). The ECM deposited in the non-labeled hydrogels occurred in cloudy patches, whereas irregular stripes filling the mesh were observed in the USPIO-labeled groups. These results indicate that the USPIO-labeled CNC/SF hydrogel provides a suitable, noncytotoxic environment for BMSC chondrogenesis *in vitro*.

The expression levels of cartilage-specific marker genes (encoding collagen II, aggrecan, and Sox9) and a dedifferentiation-related gene (collagen I) in the non-labeled and USPIO-labeled CNC/SF hydrogels were also evaluated (Figure S2B). Collagen II expression was significantly upregulated over time, whereas aggrecan and Sox9 were expressed strongly on day 14 but downregulated thereafter on day 28. The expression of collagen I remained constant over time in the USPIO-labeled CNC/SF hydrogel, whereas it was significantly upregulated in the non-labeled CNC/SF hydrogels. Therefore, the

hydrogel with incorporated USPIO was suitable for BMSC chondrogenesis *in vitro*, and did not promote the fibrocartilage phenotype.

### Stability of the labeled CNC/SF hydrogels during *in vitro* chondrogenesis

To investigate the imaging stability during chondrogenesis *in vitro*, USPIO-labeled CNC/SF hydrogels with and without encapsulated BMSCs were monitored with T2 mapping and T2\* mapping scanning sequences to determine the corresponding R2 and R2\* values, respectively. No significant changes in the relaxation rate were observed over time in either group, and no difference between the groups was observed (Figure 4E). Generally, the relaxation rate is proportional to the iron content and inversely proportional to the calcium content. On one

hand, the unaltered relaxation rate indicated that the amount of hydrogel degradation due to the enzymes secreted by BMSCs, which could lead to a reduction in relaxation rate, was not significant during *in vitro* chondrogenesis in 4 weeks. On the other hand, no obvious matrix mineralization through endochondral ossification resulting in an increased relaxation rate, was observed during *in vitro* culture. These results demonstrate that USPIO-labeled hydrogels retain their stability with no loss of the relaxation rate, satisfying the necessary imaging property for visualization or quantitation during *in vitro* incubation for a month. Therefore, the USPIO-labeled hydrogel, even when precultured with BMSCs, has great potential utility for monitoring chondrogenesis with high stability.

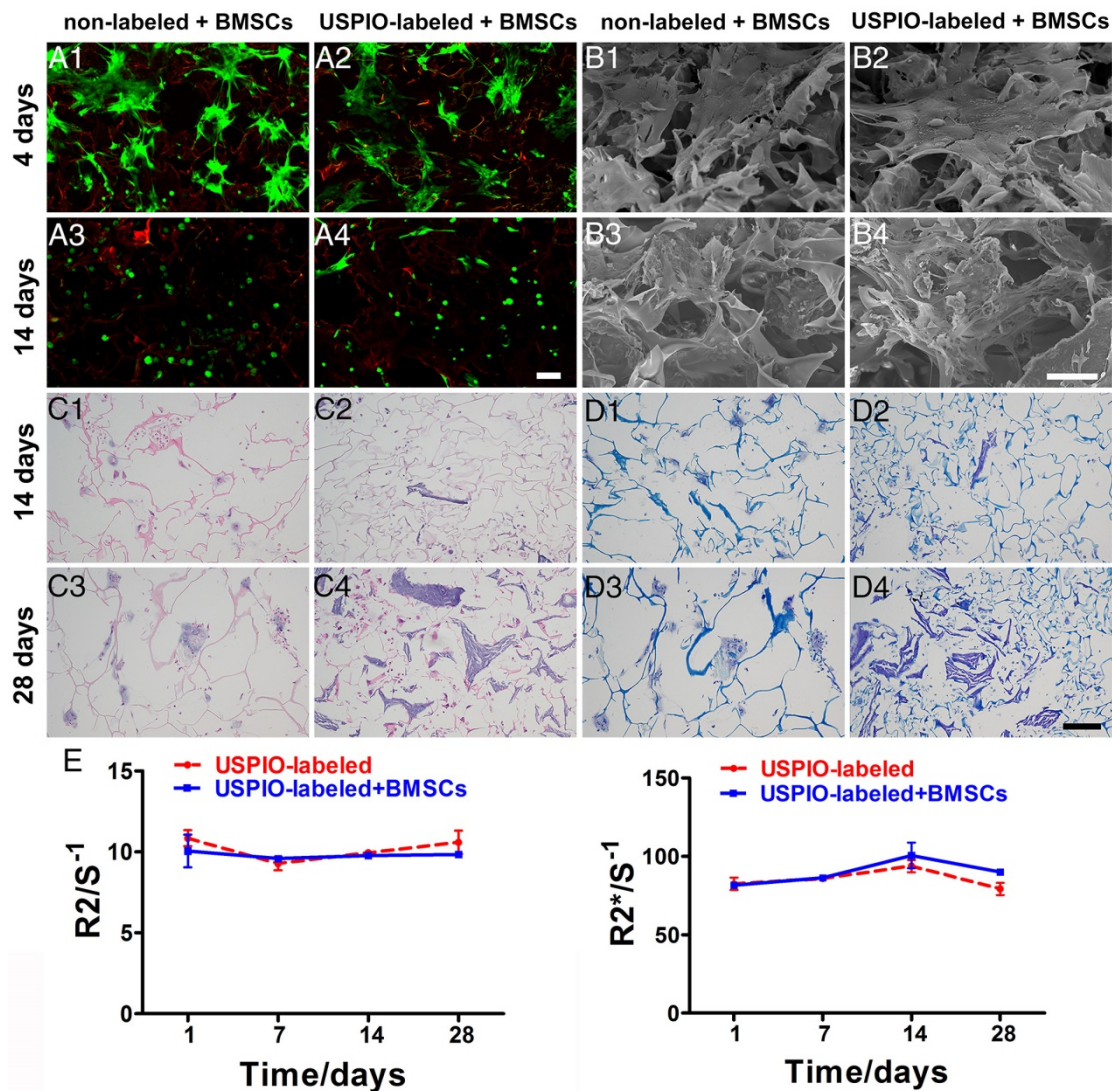


**Figure 4.** Biocompatibility, histological analysis, and imaging stability of non-labeled and 0.1% (w/w) USPIO-labeled CNC/SF hydrogels loaded with BMSCs during chondrogenesis *in vitro*. (A) Live/dead assay was used to evaluate cell survival on day 4 (A1, A2) and day 14 (A3, A4). Scale bar indicates 100  $\mu$ m. (B) Representative SEM of cocultured constructs on day 4 (B1, B2) and day 14 (B3, B4). Scale bar indicates 50  $\mu$ m on day 4 and 100  $\mu$ m on day 14. (C) H&E staining for histomorphometric analysis on day 14 (C1, C2) and day 28 (C3, C4). (D) Toluidine blue staining to assess cartilage-specific ECM deposition on day 14 (D1, D2) and day 28 (D3, D4). Scale bar indicates 100  $\mu$ m. (E) R2 and R2\* relaxometry rate measurements indicated stable MRI visualization of the USPIO-labeled hydrogels over one month.

## MR and histological evaluation of the hydrogel degradation *in vivo*

Finally, the initial proof of principle for monitoring hydrogel degradation and cartilage regeneration in a rabbit cartilage defect model *in situ* was demonstrated with multiparametric MRI and confirmed with a conventional histological analysis.

The real-time dynamic degradation of the implanted hydrogels was monitored for 3 months with proton-density-weighted imaging (PDWI), T2 mapping, and T2\* mapping. The MR signal intensity in USPIO-labeled groups gradually decreased, whereas the signal intensity remained unchanged in the two non-labeled groups macroscopically (Figure 5A). The R2 and R2\* values were calculated to evaluate the degree of degradation of the implanted hydrogels (Figure 5B). Different trends of the relaxation rate were found between USPIO-labeled CNC/SF hydrogels with and without BMSCs. R2 and R2\* increased gradually in the non-labeled group with or without BMSC loading. In contrast, a clear declining trend in the relaxation rate was observed in the USPIO-labeled group without BMSC loading. The increased relaxation rate in non-labeled acellular hydrogels may be due to calcium deposited in subchondral bone. However, in the USPIO-labeled acellular hydrogels, the decreasing relaxation rate caused by reduced oxide iron particles might outweigh this factor, as shown in non-labeled acellular hydrogels. Therefore, the trends observed in non-labeled and USPIO-labeled acellular scaffolds are opposite. Additionally, an interesting turning point in the relaxation rate was detected in the USPIO-labeled group loaded with BMSCs during repair in week 8 (Figure 5B). For example, R2 was lower in week 8 post-implantation ( $13.1 \text{ s}^{-1}$ ) than in week 4 or 12 ( $15.7 \text{ s}^{-1}$  or  $18.5 \text{ s}^{-1}$ , respectively), whereas R2\* was  $57.6 \text{ s}^{-1}$  in week 8, but  $82.2 \text{ s}^{-1}$  and  $91.2 \text{ s}^{-1}$  in weeks 4 and 12, respectively. This *in vivo* relaxation rate trend was probably related to the complicated tissue engineering strategy including hydrogel absorption and neotissue replacement. On one hand, the *in vivo* hydrogel degradation might be attributed to phagocytosis, as demonstrated by Wang and coworkers.<sup>[46]</sup> Iron particles might be taken up by macrophages and released into the circulatory system, which resulted in the decreasing relaxation rate. On the other hand, the calcium deposited in subchondral bone might increase the relaxation rate.<sup>[47]</sup> Therefore, the result reflected the comprehensive process due to both factors in hydrogel absorption and neotissue replacement at different time points.

The process of biomaterial absorption detected with MRI was confirmed with conventional H&E (Figure 5C) and Prussian blue staining (Figure 5D). H&E distinguished the morphological changes in the implanted hydrogels. In week 4, all the rectangular constructs clearly filled each defect site. In week 8, the hydrogels in the groups seeded with BMSCs were absorbed more quickly than the control groups implanted with hydrogels alone. Finally, in week 12, small amounts of hydrogels encapsulating BMSCs remained, with far better osteochondral tissue regeneration with matrix mineralization, resulting in an increased relaxation rate.<sup>[47]</sup> We speculate that matrix mineralization through endochondral ossification in subchondral bone might be one reason for the regeneration, and partial endogenous or exogenous BMSCs might join osteogenic differentiation and secrete the ECM for subchondral bone reconstruction in the complicated *in vivo* environment. Prussian blue staining showed that the USPIO distribution was similar in the labeled groups both with and without BMSCs in week 4, which was reflected in their similar relaxation rates. In week 8, more strongly stained iron particles, corresponding to higher relaxation rates, were observed in the labeled group without seeded BMSCs, whereas only a few scattered blue spots were observed in the USPIO-labeled hydrogels loaded with BMSCs. Finally, in week 12, more positively stained spots were still present in the USPIO-labeled groups without encapsulated BMSCs, which might explain the continuous decline in the relaxation rate reported above.

## MR, macroscopic and histological evaluation of cartilage regeneration *in vivo*

A noninvasive morphological evaluation of the neocartilage was performed with MRI 3D water-selective cartilage scan (3D\_WATSc) sequences, a clinical technique with short scanning time and high signal contrast (Figure 6A).<sup>[48-50]</sup> In week 8, in the groups treated with BMSC-loaded hydrogels, marginal hyperintense signal attributed to neocartilage extended into the defects, along the adjacent normal articular cartilage. Moreover, smooth and continuous articular cartilage was clearly identified in week 12. Notably, there was no significant difference in regeneration efficiency in the groups implanted with non-labeled or USPIO-labeled BMSC-loaded hydrogels. However, a small defect on the cartilage surface was still observed in week 12 in the control groups treated with hydrogel alone. As expected, the BMSC-loaded hydrogels showed enormous potential utility for cartilage repair.

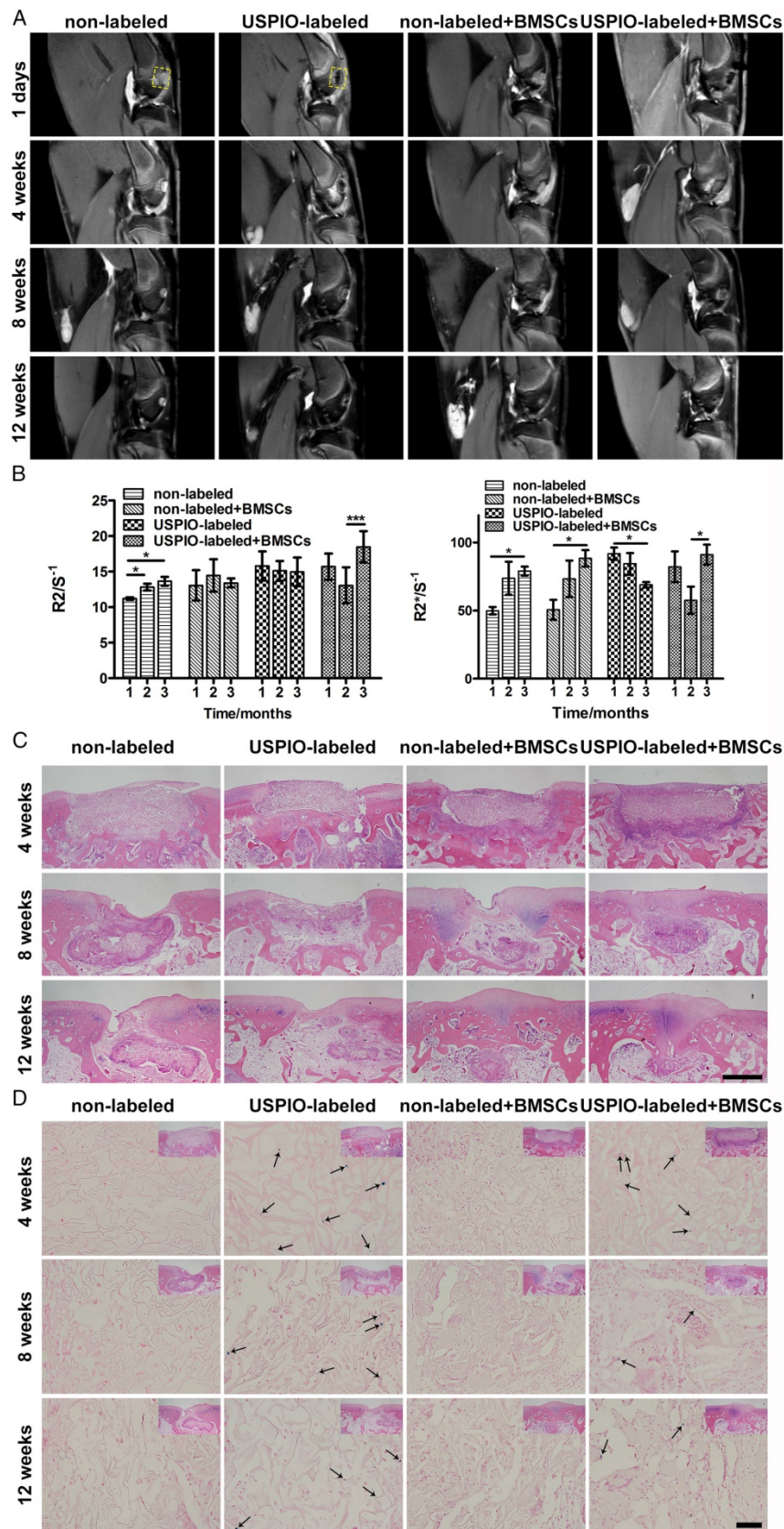


**Figure 5.** MRI and histological analysis of the *in vivo* degradation of non-labeled and 0.1% (w/w) USPIO-labeled CNC/SF hydrogels in a rabbit cartilage defect model. (A) Proton-density-weighted imaging was used for the morphological observation of tissue engineering constructs. (B) Semiquantitative  $R2$  and  $R2^*$  relaxometry rate comparison between different hydrogel constructs. (C) H&E staining revealed dynamic changes in the implanted hydrogel constructs. Scale bar indicates 500  $\mu\text{m}$ . (D) Prussian blue staining demonstrated that USPIO particles (arrow) decreased over time and were fewer in the USPIO-labeled group loaded with BMSCs. Scale bar indicates 50  $\mu\text{m}$ .

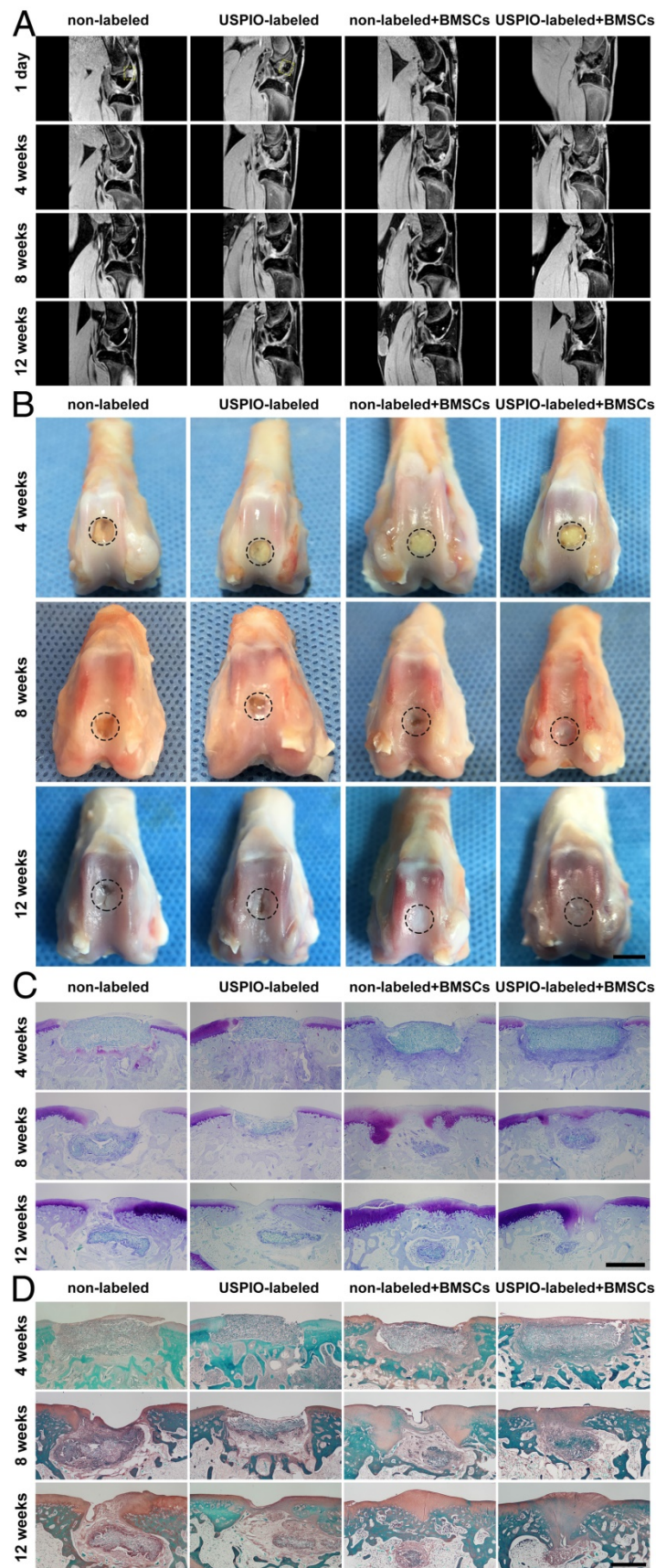


**Figure 6.** MRI, macroscopic, and histological evaluations of *in vivo* cartilage regeneration in non-labeled and 0.1% (w/w) USPIO-labeled CNC/SF hydrogels in a rabbit cartilage defect model. (A) MR 3D water-selective cartilage scan sequence for neocartilage assessment at 1 day and 4, 8, and 12 weeks after surgery. (B) Macroscopic appearance of the whole cartilage generation process. Scale bar indicates 5 mm. (C) Toluidine blue and (D) Safranin O staining showed that more cartilage-specific ECM was deposited in the regenerated cartilaginous areas in the BMSC-loaded groups. Scale bar indicates 500  $\mu$ m.

Gross images of the femoral condyles were obtained in weeks 4, 8, and 12 (Figure 6B). In week 4, yellowish residual hydrogel was clearly observed in each group, with no marginal tissue repair. In week 8, the defects in the groups treated with the BMSC-loaded hydrogels were partly repaired with thick and irregular neocartilage, which was well integrated into the adjacent host cartilage. However, yellowish hydrogel was still visible in the groups not seeded with BMSCs. In week 12, the defects were smoothly restored and integrated, with no ambient cartilage degeneration in the BMSC-loaded groups, whereas incomplete repair Gross images of the femoral condyles were obtained in weeks 4, 8, and 12 (Figure 6B). In week 4, yellowish residual hydrogel was clearly observed in each group, with no marginal tissue repair. In week 8, the defects in the groups treated with the BMSC-loaded hydrogels were partly repaired with thick and irregular neocartilage, which was well integrated into the adjacent host cartilage. However, yellowish hydrogel was still visible in the groups not seeded with BMSCs. In week 12, the defects were smoothly restored and integrated, with no ambient cartilage degeneration in the BMSC-loaded groups, whereas incomplete repair with irregular central cracking was observed in the groups filled with hydrogel alone. The International Cartilage Repair Society (ICRS) macroscopic scores were calculated to evaluate the repaired cartilage.<sup>[51]</sup> The groups treated with BMSC-loaded hydrogels had significantly higher scores than the control groups implanted with hydrogel alone (Figure S3).

Toluidine blue and Safranin O staining were used to verify the formation of cartilage-specific ECM (Figure 6C, D). No typical hyaline cartilage was formed in week 4 in any group. After 12 weeks, the hydrogels loaded with BMSCs showed successful cartilage regeneration, although the cartilage was not as well integrated as native cartilage. Fibrous tissue with no positive staining filled the defects in the control groups implanted with hydrogel alone, indicating that the cartilage had limited endogenous regenerative ability. No significant difference in the neocartilage was detected microscopically between the groups treated with non-labeled and USPIO-labeled hydrogels at different time points.

Different biomedical imaging methods are available to assess tissue-engineered strategies. Fluorescence imaging is restricted by fluorescence penetration depth and intractable photobleaching<sup>[52]</sup>, and computed tomography is limited by soft tissue contrast and ionizing radiation, but MRI can be superior to provide morphological, functional, and molecular information together due to multiple sequences<sup>[18]</sup>. In our work, USPIO labeling showed no

detrimental effects on the structural properties or long-term biocompatibility of CNC/SF hydrogel for chondrogenesis. A semiquantitative evaluation of biomaterial degradation and a morphological analysis of the regenerated cartilage using multiparametric MRI were consistent with our histological observations. However, this study suffered several limitations. First, the USPIO incorporated in the hydrogels may interfere with the magnetic field uniformity, which makes it difficult to evaluate the neotissue regeneration by other functional MR sequences, such as T1 $\rho$ , CEST or <sup>23</sup>Na MR, for cartilage-specific ECM quantification. Second, the animal used in this study was relatively small, which may limit generalization of our results. Third, further study is needed to explore the effect of USPIO concentration on hydrogel cross-linking and growth factors delivery.

## Conclusion

In summary, this work presents a novel functional hydrogel system fabricated from USPIO-labeled CNC/SF hydrogel, which not only provides favorable MRI contrast, mechanical properties, and biocompatibility, but also allows the noninvasive visualization and semiquantitative analysis of hydrogel degradation and cartilage regeneration *in situ*. The *in vivo* degradation of the hydrogel constructs was monitored longitudinally using MRI relaxation rate measurements, and the neocartilage was assessed simultaneously with 3D\_WATSc sequences. This USPIO-labeled CNC/SF hydrogel with cocultured BMSCs should provide a practical approach to monitoring hydrogel degradation noninvasively and effectively promote cartilage regeneration.

## Experimental Section

*Materials:* *Bombyx mori* silk cocoons were kindly provided by Zhejiang University (Zhejiang Province, China). Microcrystalline cellulose (MCC, 50  $\mu$ m) and FeCl<sub>2</sub>·4H<sub>2</sub>O were from Aladdin Reagents Co. Ltd (Shanghai, China).  $\alpha$ -Minimal essential medium ( $\alpha$ -MEM), fetal bovine serum (FBS), penicillin-streptomycin, phosphate-buffered saline (PBS), and chondrogenic medium were from Gibco (Grand Island, NY, USA). The Cell Counting Kit-8 was from Dojindo (Kumamoto, Japan) and the LIVE/DEAD™ Cell Imaging Kit was from Invitrogen (Carlsbad, CA, USA). TRIzol Reagent, PrimeScript™ RT Master Mix, and SYBR® Premix Ex Taq™ were from Takara Bio (Kyoto, Japan). All other chemicals were of analytical grade, were purchased from Sigma-Aldrich (St. Louis, MO, USA), and were used without further purification.

*Synthesis of 3D porous USPIO/CNC/SF hydrogels:* Briefly, CNCs and USPIO ranging from 0.1%–0.6% (w/w) were dispersed in 1 mL of deionized water with sonication. Then 6% SF solution (9 mL) was slowly added with vigorous vortex mixing. The sol-gel transition of the mixture occurred at room temperature. For in vitro experiments, 150  $\mu$ L of the solution was pipetted into 96-well plates, frozen at  $-20$  °C overnight, and lyophilized for 36 h. All hydrogels were sterilized with  $^{60}\text{Co}$  irradiation before cell encapsulation.

*Morphology:* After the freeze-dried hydrogels (CNC/SF with 0–0.6% (w/w) USPIO) were sputter-coated with gold, the morphology of their porous structures and the interconnectivity within the hydrogels were observed with SEM (XL-30; Philips, Best, The Netherlands) at an operating voltage of 20 kV.

*MR properties and imaging stability in vitro:* T2-weighted imaging (T2WI) was performed and the relaxation rate properties were measured for all the prepared untreated hydrogels (0–0.6% (w/w) USPIO) in a clinical 3 T whole-body MR scanner (Philips Achieva, Best, The Netherlands), using an eight-channel head coil (SENSE-flex-M; Philips, Best, The Netherlands). The relaxation rates of the pretreated hydrogels, with and without BMSCs, cocultured in chondrogenic medium were calculated weekly for 28 days. All samples were embedded in 1% (w/v) agarose gel and subjected to T2WI, T2 mapping, and T2\* mapping sequences. The T2WI acquisition parameters were: TR = 5000 ms, TE = 5.8 ms, FOV = 8 mm  $\times$  8 mm, matrix size = 64  $\times$  64, in-plane resolution = 125 mm  $\times$  125 mm, and slice thickness = 0.8 mm. The acquisition parameters for transverse (T2) relaxation times were: TR = 1500 ms, TE = 8–48 ms, number of echoes = 6, inter-echo spacing = 8 ms, reconstruction matrix = 288, voxel size = 0.6  $\times$  0.6, slice thickness = 1 mm, and scan mode = multi-shot. The acquisition parameters for transverse (T2\*) relaxation times were: TR = 733 ms, TE = 5.4–35.1 ms, number of echoes = 6, FOV = 40 mm  $\times$  40 mm, reconstruction matrix = 112, voxel size = 0.4  $\times$  0.4 mm, slice thickness = 0.8 mm, and flip angle = 45°. The T2 and T2\* relaxation times were calculated by fitting the signal intensities to an exponential curve as a function of the echo time (TE) based on the regions of interest in the hydrogels using the ImaLytics Preclinical Software (Philips Technology GmbH, Aachen, Germany).

*Biocompatibility:* The morphologies of non-labeled CNC/SF and 0.1% (w/w) USPIO-labeled hydrogel constructs incubated with BMSCs were observed with SEM (Hitachi, S-3000N, Japan) on day 4 and day 14 post-implantation. After the samples were

washed twice with PBS, they were fixed in 2.5% glutaraldehyde, dehydrated through a graded series of ethanol, critical-point dried, and sputter-coated with gold before observation. Cell viability in the hydrogel constructs (CNC/SF and 0.1% (w/w) USPIO/CNC/SF) at 4 and 14 days after seeding was determined with a live/dead assay. Live cells stained with calcein presenting green fluorescence, and dead cells stained with ethidium homodimer-1 presenting red fluorescence, were distinguished with a confocal laser scanning microscope (Olympus FluoView™ FV10i, Tokyo, Japan).

*ICP-MS analysis:* All the prepared hydrogels (CNC/SF with 0%–0.6% (w/w) USPIO) were digested in a closed-vessel microwave reaction system after the addition of 2.5 mL of 65 wt% nitric acid to 0.5 mL of 30 wt% hydrogen peroxide at 155 °C overnight. The samples were diluted 1:20 in deionized water. The amount of incorporated iron was determined with high-resolution sector field ICP-MS (Optima 2000 DV, Perkin Elmer, New York, USA).

*Prussian blue staining:* The incorporation and distribution of the USPIO nanoparticles within the 0–0.6% (w/w) USPIO-labeled hydrogels were determined with Prussian blue staining. Paraffin sections were incubated with Prussian blue solution (5% hydrochloric acid and 5% potassium ferrocyanide) for 10 min and counterstained with Nuclear Fast Red for 5 min.

*Characterization of the hydrogels:* To detect the functional chemical bonds and interactions in the composite hydrogels (SF, CNC, USPIO, CNC/SF, 0.1% (w/w) USPIO/CNC/SF), their infrared spectra were determined on an FT-IR spectrometer (Vertex 70, Bruker, Germany) in the range of 400–4000  $\text{cm}^{-1}$  with the accumulation of 20 scans with a resolution of 4  $\text{cm}^{-1}$ . The tested samples were prepared with the KBr-disk method.

The mechanical properties of the samples (SF, CNC/SF, 0.1% (w/w) USPIO/CNC/SF) were determined with unconfined compression on a mechanical testing apparatus (MTS QT/1L, MTS Systems Corporation, USA) at a 1 mm/min strain rate. The compression distance was 3.5 mm. The raw data were recorded as force *versus* displacement and converted to stress *versus* strain with respect to the initial dimensions.

The enzymatic degradation of the hydrogels (SF, CNC/SF, 0.1% (w/w) USPIO/CNC/SF) was determined with protease XIV, with an activity of  $\geq 3.5$  units/mg. The hydrogels were immersed in 1 mL of protease solution for 7 days at the ambient temperature. The degradation rate was calculated with the following equation: degradation (%) =  $(w_i - w_t) / w_i \times 100\%$ , where  $W_i$  is the initial hydrogel

weight and Wt is the hydrogel weight after specified time intervals.

The thermostability of the polymeric blends (SF, CNC, CNC/SF, 0.1% (w/w) USPIO/CNC/SF) was determined on a thermogravimetric instrument (209F3Tarsus, Netzsch, Germany). Samples weighing 4–6 mg were placed in clean platinum pans and scanned at a heating rate of 10 °C/min. The heating temperature range was 35–800 °C under a 60 mL/min flow of nitrogen.

**Histological analysis:** Non-labeled and 0.1% (w/w) USPIO-labeled hydrogels cocultured with BMSCs *in vitro* were collected in weeks 2 and 4. *In vivo* rabbit specimens were collected for regeneration assessment in weeks 4, 8, and 12. All the specimens were fixed in 4% paraformaldehyde, decalcified in 10% ethylenediaminetetraacetic acid (EDTA) solution (rabbit specimens only), embedded in paraffin, and cut into 5 µm sections in the mid-sagittal plane. The slides were stained with H&E for morphological analysis, Prussian blue for iron oxide detection, and Safranin O and toluidine blue for cartilage-specific ECM deposition. The histological images were obtained in triplicate for each group under a light microscope (Olympus BX51).

***In vivo* MRI evaluation:** All animal procedures were approved by Institutional Animal Care and Use committee of Nanfang Hospital, Southern Medical University. All animals were subjected to 3D\_WATSc sequences, PDWI, and T2 and T2\* mapping at 1 day, and 4, 8, and 12 weeks after surgery using the MRI facilities described for the *in vitro* experiment. The 3D\_WATSc sequence acquisition parameters were: TR = 11 ms, TE = 5.4 ms, FOV = 40 mm × 40 mm, matrix size = 100 × 100, in-plane resolution = 125 mm × 125 mm, slices = 64 mm, and flip angle = 15°. The PDWI acquisition parameters were: TR = 2000 ms, TE = 36 ms, FOV = 60 mm × 60 mm, matrix size = 150 × 150, in-plane resolution = 125 mm × 125 mm, slice thickness = 0.8 mm, and flip angle = 90°. The transverse (T2) relaxation times and transverse (T2\*) relaxation times were acquired as in the *in vitro* MR experiments described above.

**Statistical analysis:** All results are given as mean ± standard deviations (SD) and all experiments were performed at least in triplicate. All values were calculated with the SPSS software (version 20.0, IBM, USA). Differences in *in vitro* experiments were evaluated with one-way analysis of variance (ANOVA), followed by Bonferroni's *post hoc* multiple-comparisons test, whereas differences in *in vivo* experiments were evaluated with repeated-measurement ANOVA. Significant differences are given as \**p* < 0.05, \*\**p* < 0.01, or \*\*\**p* < 0.001.

## Abbreviations

3D: three-dimensional; 3D\_WATSc: 3D water-selective cartilage scan; ANOVA: one-way analysis of variance BMSCs: bone-marrow mesenchymal stem cells; CEST: chemical exchange saturation transfer; CNC: cellulose nanocrystal; CTE: cartilage tissue engineering; ECM: extracellular matrix; EDTA: ethylenediaminetetraacetic acid; FBS: fetal bovine serum; FT-IR: fourier transform infrared spectroscopy; GAG: glycosaminoglycan; H&E: hematoxylin–eosin; ICP-MS: inductively coupled plasma mass spectrometry; ICRS: international cartilage repair society; MCC: microcrystalline cellulose; α-MEM: α-minimal essential medium; MRI: magnetic resonance imaging; PDWI: proton-density-weighted imaging; PBS: phosphate-buffered saline; SD: standard deviations; SEM: scanning electron microscopy; SF: silk fibroin; T2WI: T2-weighted imaging; TE: echo time; TEM: transmission electron microscopy; USPIO: ultrasmall superparamagnetic iron oxide.

## Acknowledgments

This work was financially supported by the National Natural Science Foundation of China (No. 81271642), the Science and Technology Program of Guangzhou (201601010270), Science and Technology Planning Project of Guangdong Province, China (No.2015B010131011), National Key Research and Development Program of China (No.2016YFC 0107104) and President Foundation of Nanfang Hospital, Southern Medical University (No. 2016Z018 and 2016C014). We are grateful to Dr. Yingjie Mei for providing technical support.

## Supplementary Material

Supplementary figures and tables.

<http://www.thno.org/v08p1146s1.pdf>

## Competing Interests

The authors have declared that no competing interest exists.

## References

- Makris EA, Gomoll AH, Malizos KN, Hu JC, Athanasiou KA. Repair and tissue engineering techniques for articular cartilage. *Nat Rev Rheumatol*. 2015; 11: 21-34.
- Huang BJ, Hu JC, Athanasiou KA. Cell-based tissue engineering strategies used in the clinical repair of articular cartilage. *Biomaterials*. 2016; 98: 1-22.
- Li MH, Xiao R, Li JB, Zhu Q. Regenerative approaches for cartilage repair in the treatment of osteoarthritis. *Osteoarthritis Cartilage*. 2017; 25: 1577-87.
- Bhattacharjee M, Coburn J, Centola M, Murab S, Barbero A, Kaplan DL, et al. Tissue engineering strategies to study cartilage development, degeneration and regeneration. *Adv Drug Deliv Rev*. 2015; 84: 107-22.
- Madeira C, Santhaganam A, Salgueiro JB, Cabral JM. Advanced cell therapies for articular cartilage regeneration. *Trends Biotechnol*. 2015; 33: 35-42.
- Daly AC, Freeman FE, Gonzalez-Fernandez T, Critchley SE, Nulty J, Kelly DJ. 3D Bioprinting for Cartilage and Osteochondral Tissue Engineering. *Adv Healthc Mater*. 2017; [Epub ahead of print].

7. Hanjaya-Putra D, Wong KT, Hirotsu K, Khetan S, Burdick JA, Gerecht S. Spatial control of cell-mediated degradation to regulate vasculogenesis and angiogenesis in hyaluronan hydrogels. *Biomaterials*. 2012; 33: 6123-31.
8. Dhote V, Vernerey FJ. Mathematical model of the role of degradation on matrix development in hydrogel scaffold. *Biomech Model Mechanobiol*. 2014; 13: 167-83.
9. Haider MA, Olander JE, Arnold RF, Marous DR, McLamb AJ, Thompson KC, et al. A phenomenological mixture model for biosynthesis and linking of cartilage extracellular matrix in scaffolds seeded with chondrocytes. *Biomech Model Mechanobiol*. 2011; 10: 915-24.
10. Akalp U, Bryant SJ, Vernerey FJ. Tuning tissue growth with scaffold degradation in enzyme-sensitive hydrogels: a mathematical model. *Soft Matter*. 2016; 12: 7505-20.
11. Zhu J, Marchant RE. Design properties of hydrogel tissue-engineering scaffolds. *Expert Rev Med Devices*. 2011; 8: 607-26.
12. Huey DJ, Hu JC, Athanasiou KA. Unlike bone, cartilage regeneration remains elusive. *Science*. 2012; 338: 917-21.
13. Shi D, Xu X, Ye Y, Song K, Cheng Y, Di J, et al. Photo-Cross-Linked Scaffold with Kartogenin-Encapsulated Nanoparticles for Cartilage Regeneration. *ACS Nano*. 2016; 10: 1292-9.
14. Chuah YJ, Peck Y, Lau JE, Hee HT, Wang DA. Hydrogel based cartilaginous tissue regeneration: recent insights and technologies. *Biomater Sci*. 2017; 5: 613-31.
15. Yang J, Zhang YS, Yue K, Khademhosseini A. Cell-laden hydrogels for osteochondral and cartilage tissue engineering. *Acta Biomater*. 2017; 57: 1-25.
16. Zhang Y, Rossi F, Papa S, Violatto MB, Bigini P, Sorbona M, et al. Non-invasive in vitro and in vivo monitoring of degradation of fluorescently labeled hyaluronan hydrogels for tissue engineering applications. *Acta Biomater*. 2016; 30: 188-98.
17. Artzi N, Oliva N, Puron C, Shitreet S, Artzi S, bon Ramos A, et al. In vivo and in vitro tracking of erosion in biodegradable materials using non-invasive fluorescence imaging. *Nat Mater*. 2011; 10: 704-9.
18. Nam SY, Ricles LM, Suggs LJ, Emelianov SY. Imaging strategies for tissue engineering applications. *Tissue Eng Part B Rev*. 2015; 21: 88-102.
19. Kotecha M, Klatt D, Magin RL. Monitoring cartilage tissue engineering using magnetic resonance spectroscopy, imaging, and elastography. *Tissue Eng Part B Rev*. 2013; 19: 470-84.
20. Dorsey SM, McGarvey JR, Wang H, Nikou A, Arama L, Koomalsingh KJ, et al. MRI evaluation of injectable hyaluronic acid-based hydrogel therapy to limit ventricular remodeling after myocardial infarction. *Biomaterials*. 2015; 69: 65-75.
21. Jin T, Nicholls FJ, Crum WR, Ghuman H, Badylak SF, Modo M. Diamagnetic chemical exchange saturation transfer (diaCEST) affords magnetic resonance imaging of extracellular matrix hydrogel implantation in a rat model of stroke. *Biomaterials*. 2017; 113: 176-90.
22. Khalilzad-Sharghi V, Han Z, Xu H, Othman SF. MR elastography for evaluating regeneration of tissue-engineered cartilage in an ectopic mouse model. *Magn Reson Med*. 2016; 75: 1209-17.
23. Novotny JE, Turka CM, Jeong C, Wheaton AJ, Li C, Presedo A, et al. Biomechanical and magnetic resonance characteristics of a cartilage-like equivalent generated in a suspension culture. *Tissue Eng*. 2006; 12: 2755-64.
24. Cheng HL, Loai Y, Beaumont M, Farhat WA. The acellular matrix (ACM) for bladder tissue engineering: A quantitative magnetic resonance imaging study. *Magn Reson Med*. 2010; 64: 341-8.
25. Jayapaul J, Arns S, Bunker M, Weiler M, Rutherford S, Comba P, et al. In vivo evaluation of riboflavin receptor targeted fluorescent USPIO in mice with prostate cancer xenografts. *Nano Res*. 2016; 9: 1319-33.
26. Kim DH, Chen J, Omary RA, Larson AC. MRI visible drug eluting magnetic microspheres for transcatheter intra-arterial delivery to liver tumors. *Theranostics*. 2015; 5: 477-88.
27. Revia RA, Zhang M. Magnetite nanoparticles for cancer diagnosis, treatment, and treatment monitoring: recent advances. *Mater Today (Kidlington)*. 2016; 19: 157-68.
28. Bashir MR, Bhatti L, Marin D, Nelson RC. Emerging applications for ferumoxytol as a contrast agent in MRI. *J Magn Reson Imaging*. 2015; 41: 884-98.
29. Jin R, Lin B, Li D, Ai H. Superparamagnetic iron oxide nanoparticles for MR imaging and therapy: design considerations and clinical applications. *Curr Opin Pharmacol*. 2014; 18: 18-27.
30. Gauberti M, Montagne A, Quenault A, Vivien D. Molecular magnetic resonance imaging of brain-immune interactions. *Front Cell Neurosci*. 2014; 8: 389.
31. Bull E, Madani SY, Sheth R, Seifalian A, Green M, Seifalian AM. Stem cell tracking using iron oxide nanoparticles. *Int J Nanomedicine*. 2014; 9: 1641-53.
32. Mertens ME, Hermann A, Buhren A, Olde-Damink L, Mockel D, Gremse F, et al. Iron Oxide-labeled Collagen Scaffolds for Non-invasive MR Imaging in Tissue Engineering. *Adv Funct Mater*. 2014; 24: 754-62.
33. Mertens ME, Koch S, Schuster P, Wehner J, Wu Z, Gremse F, et al. USPIO-labeled textile materials for non-invasive MR imaging of tissue-engineered vascular grafts. *Biomaterials*. 2015; 39: 155-63.
34. Wang W, Tao H, Zhao Y, Sun X, Tang J, Selomulya C, et al. Implantable and Biodegradable Macroporous Iron Oxide Frameworks for Efficient Regeneration and Repair of Infarcted Heart. *Theranostics*. 2017; 7: 1966-75.
35. Shi W, Sun M, Hu X, Ren B, Cheng J, Li C, et al. Structurally and Functionally Optimized Silk-Fibroin-Gelatin Scaffold Using 3D Printing to Repair Cartilage Injury In Vitro and In Vivo. *Adv Mater*. 2017; 29. DOI: 10.1002/adma.201701089.
36. Kundu B, Rajkhowa R, Kundu SC, Wang X. Silk fibroin biomaterials for tissue regenerations. *Adv Drug Deliv Rev*. 2013; 65: 457-70.
37. Yang J, Han C. Mechanically Viscoelastic Properties of Cellulose Nanocrystals Skeleton Reinforced Hierarchical Composite Hydrogels. *ACS Appl Mater Interfaces*. 2016; 8: 25621-30.
38. You J, Cao J, Zhao Y, Zhang L, Zhou J, Chen Y. Improved Mechanical Properties and Sustained Release Behavior of Cationic Cellulose Nanocrystals Reinforced Cationic Cellulose Injectable Hydrogels. *Biomacromolecules*. 2016; 17: 2839-48.
39. Naseri N, Deepa B, Mathew AP, Oksman K, Girandon L. Nanocellulose-Based Interpenetrating Polymer Network (IPN) Hydrogels for Cartilage Applications. *Biomacromolecules*. 2016; 17: 3714-23.
40. Roeder E, Henrionnet C, Goebel JC, Gambier N, Beuf O, Grenier D, et al. Dose-response of superparamagnetic iron oxide labeling on mesenchymal stem cells chondrogenic differentiation: a multi-scale in vitro study. *PLoS One*. 2014; 9: e98451.
41. Saha S, Yang XB, Tanner S, Curran S, Wood D, Kirkham J. The effects of iron oxide incorporation on the chondrogenic potential of three human cell types. *J Tissue Eng Regen Med*. 2013; 7: 461-9.
42. Zhang Q, Lu H, Kawazoe N, Chen G. Pore size effect of collagen scaffolds on cartilage regeneration. *Acta Biomater*. 2014; 10: 2005-13.
43. Bhardwaj N, Nguyen QT, Chen AC, Kaplan DL, Sah RL, Kundu SC. Potential of 3-D tissue constructs engineered from bovine chondrocytes/silk fibroin-chitosan for in vitro cartilage tissue engineering. *Biomaterials*. 2011; 32: 5773-81.
44. Oh SH, Park IK, Kim JM, Lee JH. In vitro and in vivo characteristics of PCL scaffolds with pore size gradient fabricated by a centrifugation method. *Biomaterials*. 2007; 28: 1664-71.
45. Kim IG, Ko J, Lee HR, Do SH, Park K. Mesenchymal cells condensation-inducible mesh scaffolds for cartilage tissue engineering. *Biomaterials*. 2016; 85: 18-29.
46. Wang Y, Rudym DD, Walsh A, Abrahamsen L, Kim HJ, Kim HS, et al. In vivo degradation of three-dimensional silk fibroin scaffolds. *Biomaterials*. 2008; 29: 3415-28.
47. Peptan IA, Hong L, Xu H, Magin RL. MR assessment of osteogenic differentiation in tissue-engineered constructs. *Tissue Eng*. 2006; 12: 843-51.
48. Roemer FW, Eckstein F, Guermazi A. Magnetic resonance imaging-based semiquantitative and quantitative assessment in osteoarthritis. *Rheum Dis Clin North Am*. 2009; 35: 521-55.
49. Duc SR, Pfirrmann CW, Schmid MR, Zanetti M, Koch PP, Kalberer F, et al. Articular cartilage defects detected with 3D water-excitation true FISP: prospective comparison with sequences commonly used for knee imaging. *Radiology*. 2007; 245: 216-23.
50. Eckstein F, Cicuttini F, Raynaud JP, Waterton JC, Peterfy C. Magnetic resonance imaging (MRI) of articular cartilage in knee osteoarthritis (OA): morphological assessment. *Osteoarthritis Cartilage*. 2006; 14 (Suppl A): 46-75.
51. Li X, Ding J, Zhang Z, Yang M, Yu J, Wang J, et al. Kartogenin-Incorporated Thermogel Supports Stem Cells for Significant Cartilage Regeneration. *ACS Appl Mater Interfaces*. 2016; 8: 5148-59.
52. Wang L, Li B, Xu F, Li Y, Xu Z, Wei D, et al. Visual in vivo degradation of injectable hydrogel by real-time and non-invasive tracking using carbon nanodots as fluorescent indicator. *Biomaterials*. 2017; 145: 192-206.